Materials & Design 224 (2022) 111379

Contents lists available at ScienceDirect

Materials & Design

journal homepage: www.elsevier.com/locate/matdes

Functionally graded ultra-high temperature ceramics: From thermo-elastic numerical analysis to damage tolerant composites

Laura Silvestroni [a,*], Diego Pavan [b], Cesare Melandri [a], Diletta Sciti [a], Nicola Gilli [c], Laia Ortiz-Membrado [d], Emilio Jiménez-Piqué [d,e], Antonio Mattia Grande [b]

[a] CNR-ISSMC (former ISTEC), Institute of Science, Technology and Sustainability for Ceramics , Via Granarolo 64, 48018 Faenza, Italy
[b] Dept. of Aerospace Science and Technology, Politecnico di Milano, Via La Masa 34, 20156 Milano, Italy
[c] CNR-IMM, Inst. for Microelectronics and Microsystems, Via Gobetti 101, 40129 Bologna, Italy
[d] Dept. of Materials Science and Eng., EEBE, Univ. Politècnica de Catalunya-BarcelonaTECH, Avda. Eduard Maristany 16, 08019 Barcelona, Spain
[e] Barcelona Research Center in Multiscale Science and Eng. - Univ. Politècnica de Catalunya-BarcelonaTECH, Avda. Eduard Maristany 16, 08019 Barcelona, Spain

HIGHLIGHTS

- $(AB)_nA$ and complex asymmetric functionally graded (FG) architectures based on ZrB_2 with short Cf were prepared by hot pressing
- The composites exhibited density < 4 g/cm^3, fracture toughness of 7–10 MPa·m$^{0.5}$ from room temperature to 1500 °C
- Nanoindentation on FG scales was consistent with modulus measured on mono-reinforced materials for Cf> 20 vol%
- Thermo-elastic fields due to layering upon cooling from sintering evaluated by FEM well agreed with actual failure behavior
- Feasible and cost-effective method to explore complex architectures for FG-UHTC composites with enhanced properties

GRAPHICAL ABSTRACT

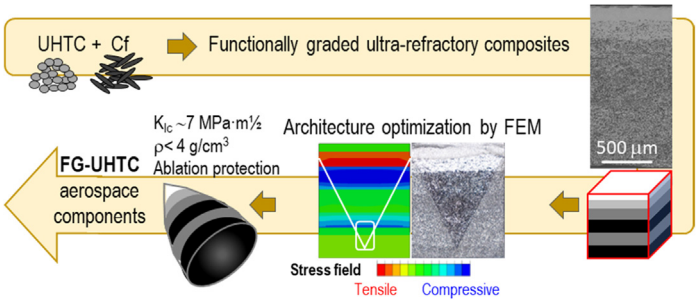

ARTICLE INFO

Article history:
Received 5 July 2022
Revised 8 November 2022
Accepted 14 November 2022
Available online 15 November 2022

Keywords:
Functionally graded composite
Finite element model
Residual stress
Toughness
Carbon fiber

ABSTRACT

To maximize the toughening contributions due to fiber bridging and residual stresses upon layering, ultra-high temperature ceramics containing variable amounts of short carbon fiber in functionally graded stacking sequences were designed and characterized. Stress fields evaluated by finite element model on $(AB)_nA$ and more complex asymmetric architectures were compared to the experimental fracture toughness pointing to an effective toughness increment in those structures where the notch fell in zones of residual compression. For the best composite, toughness at room temperature achieved 7 MPa·m$^{0.5}$ and further increased to 10 MPa·m$^{0.5}$ when tested at 1500 °C within a light ZrB_2-based composite with density below 4 g/cm^3.

According to the numerical simulations and the effective microstructural features of the composites, the main guidelines for the realization of ceramics with simultaneous failure tolerance and ablation resistance were established.

* Corresponding author.
E-mail address: laura.silvestroni@istec.cnr.it (L. Silvestroni).

https://doi.org/10.1016/j.matdes.2022.111379
0264-1275/

1. Introduction

Ultra-high temperature ceramics (UHTCs), including borides and carbides of transition metals with melting point exceeding 3000 °C, are widely recognized for their attractiveness as materials for hypersonic systems, owing to their high thermal conductivity and exceptional ablation resistance under harsh environments [1–3] that exceed the performance of conventional high temperature structural ceramics [4,5]. Broadly investigated and assessed is also the beneficial effect of the combination of borides with 10–20 vol% SiC on the thermo-mechanical properties and oxidation resistance [6,7]. However, one major aspect that continues to undermine a broader employ of these composites remains the poor fracture toughness and the catastrophic fracture these ceramics undergo in presence of flaws. Approaches undertaken so far include the addition of high aspect ratio secondary phases, like carbon nanotubes [8], whiskers, platelets, flakes and fibers [9–14]. Regarding the introduction of fibers, if well protected within the UHTC matrix and sintered under processing conditions that do not affect the fiber properties, those made of carbon have demonstrated better capability to withstand high energy fluxes over SiC fibers, which instead undergo active oxidation and leave large voids in the sub-scale thus weakening the oxide architecture [9–12]. Another route to increase the failure tolerance of ceramics, not only of borides, is to exploit the residual stresses rising upon layering of different compositions with variable thermo-elastic properties and sintering at high temperature, a methodology extensively exploited in the case of ZrO_2-Al_2O_3 ceramics [15–18].

In multi-layered composites with strong interfaces, residual stresses rise because of the differences in thermal expansion coefficient, Young's modulus, chemical reactions, and phase transformations of the layers. Coupling of layers of different thickness and composition is advantageous when the stress field at the interface enables sufficient compression/tension toughening, but not excessive development of cracks, i.e., does not exceed the fracture strength of the specific composition.

Merging the combined actions of short carbon fibers and multilayering in a functionally graded composite is a worthwhile route to mitigate the trade-off between the great strength and ablation behavior, on one side, and poor failure tolerance and high weight, on the other side, typical of UHTCs [19–21].

The combinations of powder and fiber fractions, as well as the architecture arrangements, are infinite and a numerical model that foresees the thermo-elastic fields of the sintered composite is fundamental to minimize the experimental effort. However, contrary to polymeric and metallic materials, that experience low temperature processes that do not alter the constituent fundamental properties [22–24], ceramics need consolidation treatments at very high temperature. Particularly, UHTCs need temperatures over 1750 °C to eliminate the porosity and achieve their full engineering potential. The mixture of fiber with starting boride powders, together with the oxides that naturally cover their surface, all placed in a reducing environment at high temperature trigger a series of reactions that end with different compounds as those initially batched and, in some cases, with different properties of the constituting phases, modified by the same reactive sintering environment [25]. It follows that it is not always clear and known which are the actual properties of the elements constituting the final ceramic composite and hence which are the correct parameters that have to be used for a proper design of UHTC-based aerospace structures.

In this work, for the first time, the thermo-elastic properties of ZrB_2-10 vol% SiC ceramics singularly reinforced with short carbon fiber in fractions varying from 0 to 60 vol% were experimentally measured to feed finite element analyses that describe the residual stress field in multi-layered ceramics upon cooling from the processing temperature of 1900 °C. First, $(AB)_nA$ architectures were explored, and then more realistically usable complex FG designs were investigated, these had an outermost ablation resistant UHTC pure layer and a progressively fiber-rich damage tolerant body. These structures were experimentally realized, and their fracture toughness measured up to 1500 °C to establish a correlation between residual stress state and actual capability to limit fracture propagation. In addition, to verify the effect of microstructural discrepancies in mono-reinforced standalone materials and in multilayered composites, like residual porosity or micro-cracking, nanoindentation was performed on the multi-layered structures to extract the actual stiffness and refine the numerical models.

Examination of the model's applicability and of the functionally graded architectures provides fundamental guidelines for the design of novel composites with superior properties for the aerospace field and emphasizes the invaluable support of numerical tools under the perspective of enhancing costs and time economy.

2. Experimental procedure

2.1. Materials preparation

Powder mixtures with the following compositions (in vol%) were prepared:

ZB0: ZrB_2 + 10 SiC
ZB20: (ZrB_2 + 10SiC) + 20 Cf
ZB45: (ZrB_2 + 10SiC) + 45 Cf
ZB60: (ZrB_2 + 10SiC) + 60 Cf

The following commercial powders were used for the preparation of the mixtures for the FGCs: ZrB_2 (H.C. Starck, Grade B, Germany) with particle size range 0.6–4.7 μm, impurities (wt%): C 0.2, O 0.7, N 0.10, Fe 0.1, Hf 1.7; α-SiC (H.C. Starck, Grade UF-25, Germany) with specific surface area 23–26 m^2/g, D_{50} 0.45 μm; and C chopped fibers (Granoc XN-80C-03S, Nippon Graphite Fiber, Japan) with 7–10 μm diameter and 3 mm nominal length.

Each powder and fiber mixture was ball milled for 24 h in absolute ethanol using silicon carbide media and with a rotation speed of 150 rpm. Subsequently, the slurries were dried in a rotary evaporator and the powders de-agglomerated. The dry powder mixtures were then weighed and gently poured and flattened into a 30 mm steel mold alternating different sequences according to the stacking arrangement and nomenclature displayed in Fig. 1a, b and explained in Section 2.2. The powders were uniaxially pressed at 25 MPa, perpendicularly to the fiber length, to obtain pellets with 30 mm diameter and with suitable thickness for mechanical testing, i.e., around 3–4 mm. Note that, upon processing, the fiber length was drastically reduced and therefore could be considered as "short" or "milled" fiber, with length in the order of 100–300 μm, as illustrated in Section 3.1.

Hot pressing was conducted in low vacuum (~10 Pa) using an induction-heated graphite die with a heating rate around 40 °C/min and with a uniaxial pressure of 30 MPa, which was increased to 40 MPa at 1900 °C. After a holding time of 10 min, the furnace was cooled down to 1000 °C at around 20 °C/min, then the furnace power was turned off and the specimen was allowed to cool naturally.

2.2. FGCs design

Multilayered architectures were first studied in bi-phasic systems, i.e., coupling two compositions in a $(AB)_nA$ structure, Fig. 1a, to evaluate the stress levels between layers with very dif-

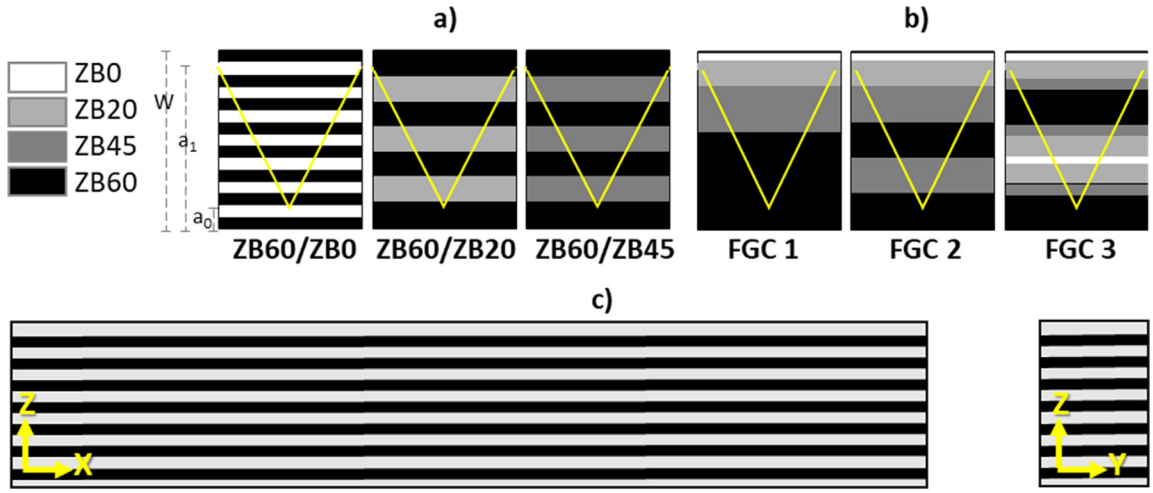

Fig. 1. a) Schematic of the $(AB)_nA$ and b) functionally graded complex architectures prepared for numerical model assessment, the yellow "V" profile marks the region where the notch is expected to fall in chevron-notch tests, W, a_1 and a_0 represent relevant length for the evaluation of the fracture toughness by chevron notch method. c) Geometry representation of the FE model for the multilayered UHTC configurations. (For interpretation of the references to colour in this figure legend, the reader is referred to the web version of this article.)

ferent or very similar properties, and then more complex geometries were considered, Fig. 1b. These last were all featured by an outermost fiber-free layer, that would provide ablation resistance, and a progressively fiber-rich body, to offer enhanced failure tolerance and lightness. As input values for the elastic modulus, the experimental ones measured on the mono-reinforced standalone materials by resonance frequency or those measured by nanoindentation on the various layers of the FGCs themselves were used and compared.

ZB60/ZB0: The greatest toughness increase due to layering is achieved when the thermo-mechanical properties are very different, i.e. by coupling a fiber-free material with a matrix containing a high volume fraction of fibre [26]. Therefore, the first computation was created by pairing *2n* layers of ZB0 (in tension) with *2n + 1* layers of ZB60 composition (in compression), where $n = 7$.

ZB60/ZB20: Assessed the critical coupling of the ZB60/ZB0 layers, simulation was employed to identify the composition containing a fiber content that would enable sufficient toughening, but not development of diffused cracking. To this aim, the subsequent multi-layered composite was composed by 7 layers alternating ZB60 and ZB20 compositions with equal thickness.

ZB60/ZB45: The next bi-phasic composite considered the critical coupling of the previous ZB60/ZB0 and ZB60/ZB20 layers and an $(AB)_nA$ architecture was conceived so to avoid micro-cracking in the layers under traction, i.e. coupling compositions with similar properties. Therefore, ZB60 and ZB45 were selected for A and B, respectively, with a total of 7 layers and thickness of each equal to 358 μm, so to obtain an overall thickness of 2.5 mm suitable for mechanical testing.

FGC 1: As variation of the published FGC [20], a graded architecture was prepared in such a way that each progressively fiber-rich composition had doubled thickness as compared to the layer above, so to dampen its traction state.

FGC 2: As further variation of the previous FGC 1, in FGC 2 the fiber-rich zone was in turn segmented into additional ZB45/ZB60 layers, to exploit the stress regime observed in correspondence of the position of the notch, likewise in the $(AB)_nA$ architectures.

FGC 3: As last more complex architecture configuration, FGC 3 was generated so to respect a gradual transition from 0 to 60 vol %, from the outermost upper surface to the core, and also to introduce a highly compressed zone in correspondence of the position of the notch, i.e., by adding a fiber-free layer in the composite core.

2.3. Materials characterization and thermo-elastic analysis

The sintered functionally graded pellets were sectioned and polished or fractured to inspect the microstructure. Optical microscopy (HIROX RH-2000, Tokyo Japan) and scanning electron microscopy (FE-SEM, Carl Zeiss Sigma NTS Gmbh, Oberkochen, DE) coupled with energy dispersive x-ray spectroscopy (EDS, INCA Energy 300, Oxford instruments, UK) were used .

Key microstructural features, like actual thickness of each layer, or characteristics of the matrix/fiber interface were evaluated using computerized image analysis (Image Pro Plus, v.7, Media Cybernetics, USA) on SEM micrographs.

The elastic constants and thermal expansion coefficient were experimentally measured on the mono-reinforced UHTCs containing 20 to 60 vol% short carbon fibers. Young's modulus, E, and Poisson's ratio, ν, were measured by the resonance frequency method on $28 \times 8 \times 0.8$ mm^3 specimens using an HP gain-phase analyzer following the European standard for advanced technical ceramics, prEN 843–2. The thermal expansion coefficient, CTE, was measured up to 1300 °C under flowing argon with a 10 °C/min heating rate, using a dilatometer Netzsch mod. DIL E 402 (Netzsch, Geraetebau, Germany) on test bars $13 \times 2.0 \times 2.5$ mm^3 (length by width by thickness, respectively).

As further test, to have a direct measure of the actual elastic values of the various compositions in the various architectures, i.e., to account for possible formation of microcracks in the FG structures, nanoindentation was carried out on the functionally graded architectures using a KLA iMicro nanoindenter (KLA Corp., USA) equipped with a Berkovich diamond tip. At least 40 indentations, with peak load of 500 mN and distance of 10 μm one from the other, were done in different positions of the same composition to investigate the indentation modulus. The indenter was continuously loaded up to the peak load with a strain rate of $\frac{\dot{h}}{h} = 0.05s^{-1}$ and immediately unloaded with no holding time. Nanohardness and indentation elastic modulus were calculated using Oliver and Pharr's method [27]. Before the tests, the area function of the indenter tip was calibrated on a standard fused silica specimen. Optical microscopy followed to ascertain that the indentations correctly fell in the target composition.

To have a term of comparison about the residual stresses developed upon layering, the 4-point fracture strength was measured on the mono-reinforced materials at room temperature and at 1500 °C

in argon, according to the EN 843–1 and ENV 820–1 European standards by fracturing five bars with dimensions of 25 mm × 2.5 mm × 2 mm (length by width by thickness, respectively) using a screw-driven load frame (Instron, 1195).

Fracture toughness (K_{Ic}) was evaluated using chevron notched beams (CNB) on both mono-reinforced and multi-layered composites. The outermost surfaces of the sintered FGCs were machined off to an appropriate depth and allow the mechanical properties on bars with standard dimensions. The bars, with dimensions of 25 mm × 2 mm × 2.5 mm (length by width by thickness, respectively), were notched with a 0.1 mm-thick diamond saw. The chevron-notch tip depth, W-a_0, and average side length, W-a_1, were about 2.25 and 0.30 mm, respectively, Fig. 1a. The notched bars were fractured in a 4-point bending device and loaded with a crosshead speed of 0.02 mm min^{-1}. The "slice model" equation of Munz et al. [28] was used to calculate K_{Ic}. Toughness was evaluated so that the notch tip was positioned as represented in Fig. 1b. In addition, for selected architectures, the fracture toughness was measured also at 1500 °C in partially protective Ar environment and under the same testing procedures adopted for room temperature tests. Before applying the load at 1500 °C, a dwell of 18 min ensured that thermal equilibrium was attained. Reported values of strength and toughness at room or high temperature are the average of at least 3 bars tested. The work of fracture (WoF) was calculated for the multi-layered composites. The total work was determined by measuring the area under the load deflection curve. The WoF was calculated by dividing the total work by the new surface area produced by fracture, i.e., twice the cross sectional area of the chevron portion of the toughness specimens.

To estimate the tensional state amongst the different layers, a finite element model was implement using ABAQUS/CAE software to create orthotropic specimens with dimension of 25 mm length, 2.0 mm width and 2.5 mm height, Fig. 1c. The models were meshed using reduced continuous three-dimensional eight nodes element (C3D8R). Boundary conditions were applied on the edges of the samples to allow displacements along the three main directions, while thermal loads were introduced as a cooling step from the sintering temperature of 1900 °C to room temperature. Furthermore, to develop the finite element model for the evaluation of the residual stresses upon cooling, experimental measured elastic constants and thermal expansion coefficients were adopted for the material constative equations taking in account the different behavior along the in-plane or out-of-plane directions.

3. Results and discussion

3.1. Microstructure of FGCs

3.1.1. $(AB)_nA$ architectures

A first ZB60/ZB0 composite composed of 15 layers with equal target thickness of 167 μm-thickness to reach the 2.5 mm specimen bar thickness, was prepared and an overall view of the sintered cross section is displayed in the optical image of Fig. 2a. Dark layers are Cf-rich ZB60, whereas bright ones are Cf-free ZB0. In some cases, the edges thickness was highly irregular, owing to the shaping route that foresees sliding of the piston to enable the deposition of the subsequent layer. This aspect, if confined to the edges, should not be considered critical, since these zones will be machined away during bars cutting. Notable diffused cracking naturally developed in the ZB0 layers, due to the tensional state that exceeded the fracture limit. Furthermore, it can be noticed that, in zones of regular thickness, Fig. 2b, the crack was correctly deflected across the different layers, whereas when wavy or irregular layers were met, Fig. 2c, the crack mostly propagated straight without any deflection. While the crack path is clearly visible in the ZB0 layer, in Cf-rich zones it is more difficult to follow, owing to similar dark contrasts. However, crack bridging was generally observed in ZB60, see the inset in Fig. 2a.

The overall microstructure of the multilayered ZB60/ZB20 composite is shown in the polished cross sections of Fig. 3. A very good adhesion was found between the layers with no delamination, large cracks nor defects at the interface. The layers thickness was in the 130–340 μm range with little variations due to manual layup of the powders, see the inset in Fig. 3b. Each layer presented the peculiar features observed in the mono-reinforced materials in terms of density, fiber distribution, matrix grain size and phase assembly. However, using InLens mode, micro-cracking was observed in the ZB20 layer, where the tensional state around the fiber summed up to the tensional state due to the layering, Fig. 3b,c. This aspect is expected to vary the actual thermo-elastic properties as compared to those measured on the mono-reinforced standalone material.

Regarding the ZB60/ZB45 composite, Fig. 4, although good homogeneity of the fiber within the matrices and blurry boundaries between the two compositions were confirmed, microstructure inspection by scanning electron microscope in Fig. 4c-d showed micro-cracking, particularly visible in InLens mode, around the fiber in any layer and little residual porosity in fiber-rich areas.

3.1.2. Complex architectures

Microstructure analysis of FGC 1 by optical microscope clearly highlighted the boundaries between compositions containing 0/20/45 vol% fibers, whereas the 45/60 interface remained more unclear, Fig. 5a. By SEM analysis, Fig. 5b-c, the interface between the various layers could be better resolved and no evident cracking was noticed. Additionally, it was confirmed the different fiber/matrix interface characteristic in presence of low (ZB20) or high (ZB45) fiber content, where SiC particles surrounded the fiber in a continuous or discontinuous way, respectively, Fig. 5d. Another feature diverging from the mono-reinforced standalone materials, was a slight residual porosity, like illustrated in the magnified SEM views of Fig. 5e, particularly marked for the fiber-free layer, were about 7 vol% porosity was measured.

Microstructure analysis of FGC 2 displayed in Fig. 6 shows a crack-free material, both in InLens and BSE mode and the considerations on the various layers reported for FGC 1 can be applied here too, like unclear layer separation in fiber-rich layers and suppressed micro-cracking in presence of residual porosity.

The microstructure analysis of the complex FGC 3 revealed instead diffused micro-cracking in the outmost ZB0 layer, partially mitigated in the fiber-rich layers and reappearing the ZB0 core, as evidenced in Fig. 7.

As verification of the processing route goodness, measures of each layer thickness in the complex FGCs were taken on polished SEM sections and plotted in Fig. 8, where the red spots mark the designed thickness. Within the experimental error and variability, a rather good agreement can be assessed in all cases.

3.2. Thermo-mechanical characterization

3.2.1. Mono-reinforced composites

Experimental mechanical characterization carried on mono-reinforced composites is summarized in Table 1, whereas the local stiffness of the various layers in the FGCs as tested by nanoindentation is reported in Table 2. Both data were used as inputs for the subsequent thermo-elastic analyses, as described in paragraph 3.3.

Looking at the property trend of the mono-reinforced materials, it can be noticed that the elastic properties dramatically decrease with the progressive introduction of fiber and, particularly, the Young's modulus even follows the same decrease as if the same

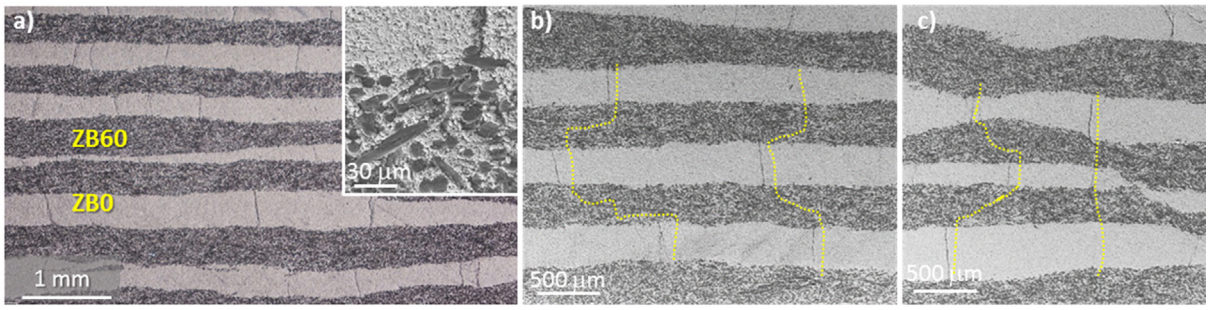

Fig. 2. a) Optical and b)-c) scanning electron microscope images of the ZB60/ZB0 composite showing a) diffused macro-cracks in the ZB0 layers with crack mode propagation inset, and b) crack path being deflected when the thickness is homogeneous or c) proceeding straight when the thickness is irregular (the yellow dotted lines guide the eye along the crack). (For interpretation of the references to colour in this figure legend, the reader is referred to the web version of this article.)

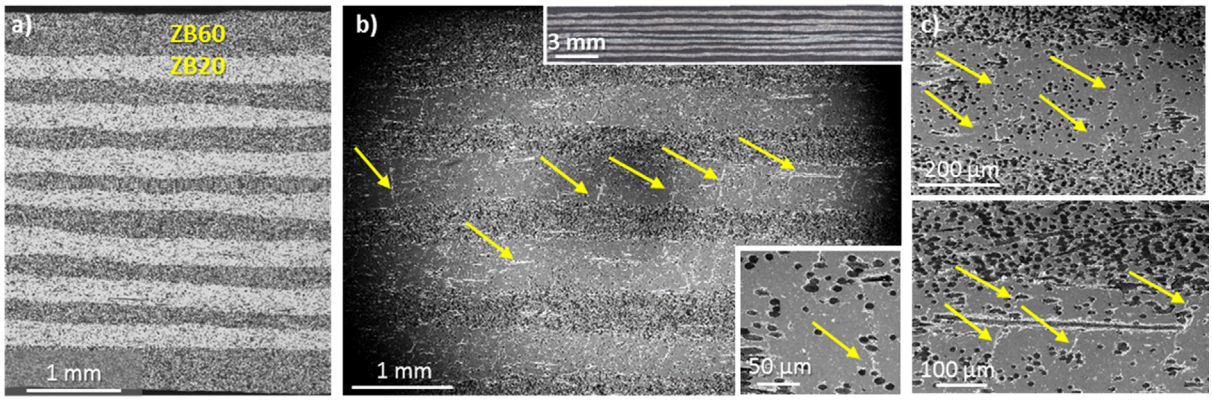

Fig. 3. Overview of the ZB60/ZB20 composite showing a) regular layer thickness, b)-c) micro-cracking in the ZB20 layers visible in InLens mode as pointed by arrows with optical image of the composite and fiber bridging inset in b).

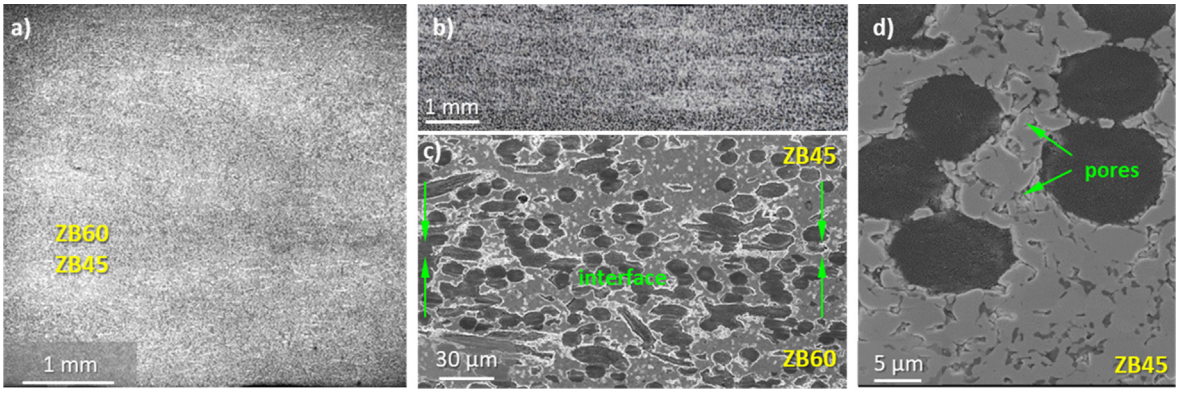

Fig. 4. a) ZB60/ZB45 composite with specimen view by b) optical microscope and corresponding SEM high magnification images showing c) blurry boundary between the two compositions, micro-cracking around the fiber (bright contrasted) and d) little residual porosity in fiber-rich zones.

volume fraction of porosity was introduced instead of fiber. This is possibly due to the weak matrix/fiber interface for fiber content above 20 vol%, see Fig. 4d.

The coefficient of thermal expansion shows a notable anisotropy owing to the orthotropy of the fiber properties [30], and the value measured along and across the fiber direction diverges always more for high fiber content.

Moreover, the room temperature fracture strength undergoes an abrupt decrease owing to a change of the defect population and increase of fiber extremities that accumulate stresses.

No notable fracture toughness increments are registered at room temperature for variable fiber contents, although all these had higher toughness as compared to the unreinforced ZB0 bulk.

On the contrary, for both strength and toughness, an increment was measured at high temperature, possibly owing to the sealing effect of the oxide scale formed during test, in analogy with similar composites [20,31].

3.2.2. Multi-layered composites

To account for microstructural discrepancies between the same composition in mono-reinforced standalone composites and in actual FGCs, nanoindentation was employed to extract more refined values of elastic modulus, Table 2.

In Fig. 9a the indentation moduli values obtained on layers of the same composition are grouped for the different composites, whereas in Fig. 9b, the modulus is plotted as a function of the layer

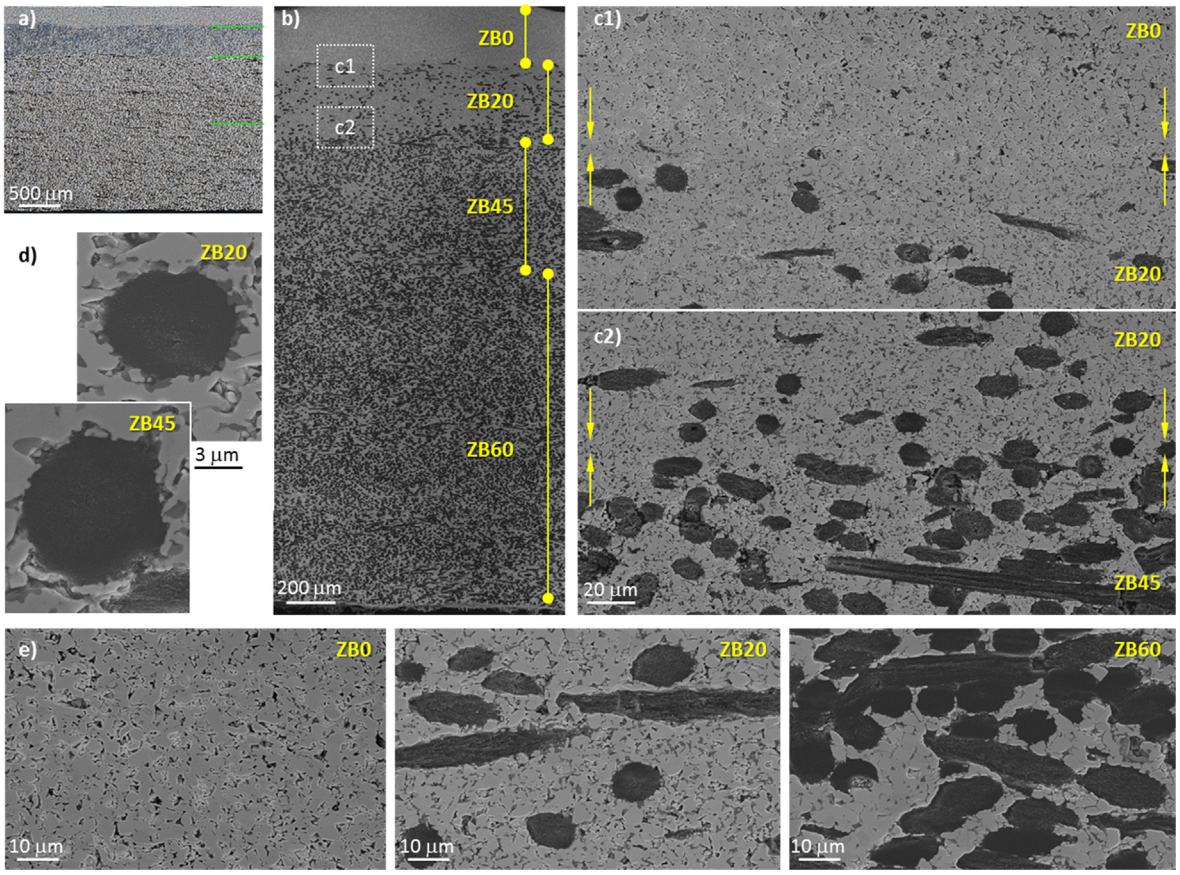

Fig. 5. a) Optical image of FGC 1 and b) corresponding SEM images highlighting the boundary between the various compositions, c) magnified views of the ZB0/ZB20 and ZB20/ZB45 critical interfaces, d) typical fiber cross sections in fiber-poor or -rich compositions with different disposition of SiC particles, e) magnified views of the microstructure in various layers showing partial residual porosity.

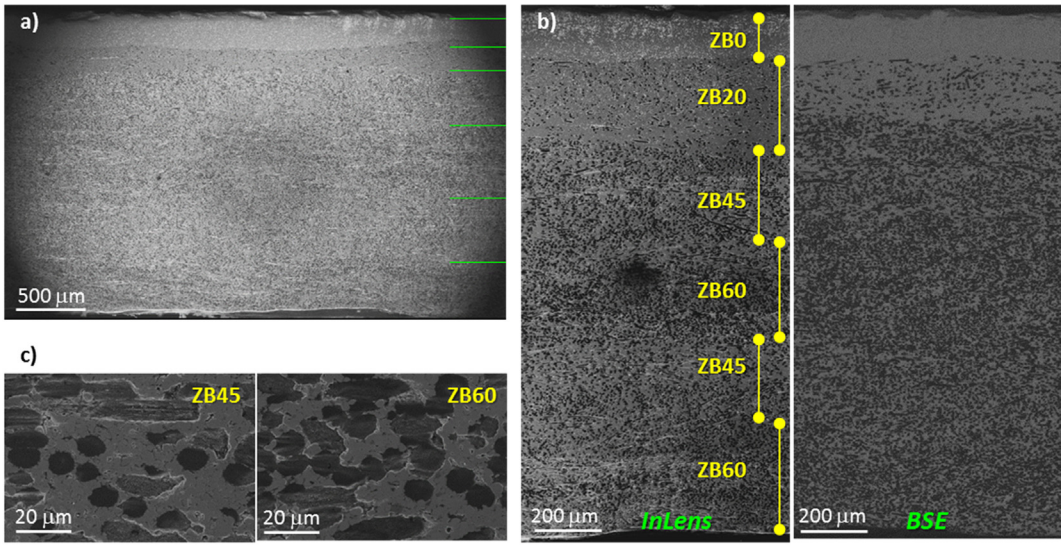

Fig. 6. a) FGC 2 cross section view by optical microscope and corresponding SEM images showing b) the boundary between the various compositions in InLens and BSE mode and c) magnified views of the fiber-rich layers.

composition within the various materials. In general, large variations are appreciable. For example, on the ZB0 composition, for which a Young's modulus exceeding 400 GPa was reported [29], values ranging from about 144 GPa, in the ZB60/ZB0 material, to 226 GPa in FGC 3 were measured. These lower values are attributable to the presence of diffused cracking and porosity, as visible in Fig. 2a-c and Fig. 5, respectively, not present instead in the single standalone unreinforced ceramic [29]. For the ZB20 composition, with a Young's modulus of 335 GPa measured on the mono-reinforced material, the discrepancy with the local properties

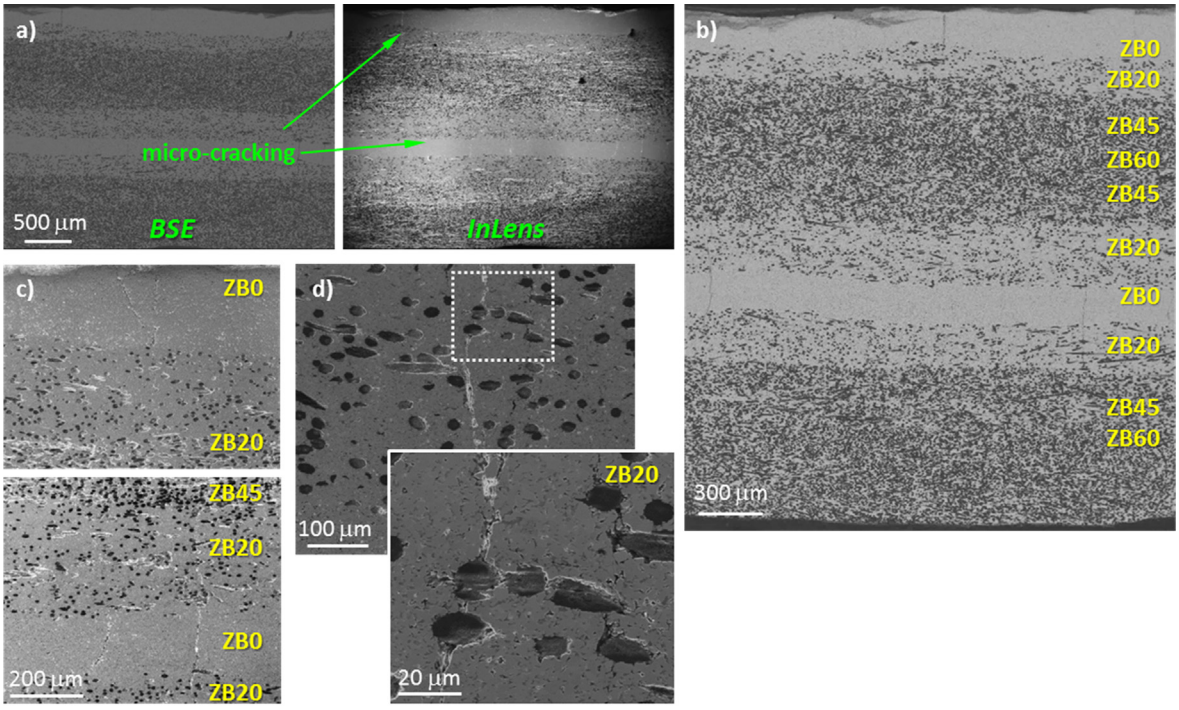

Fig. 7. a) SEM images of FGC 3 taken in BSE or InLens mode showing diffused micro-cracking, b)-c) magnified views of the microstructure highlighting cracks within the ZB0 layers and partially arrested in the fiber-rich ones, d) crack path in ZB20.

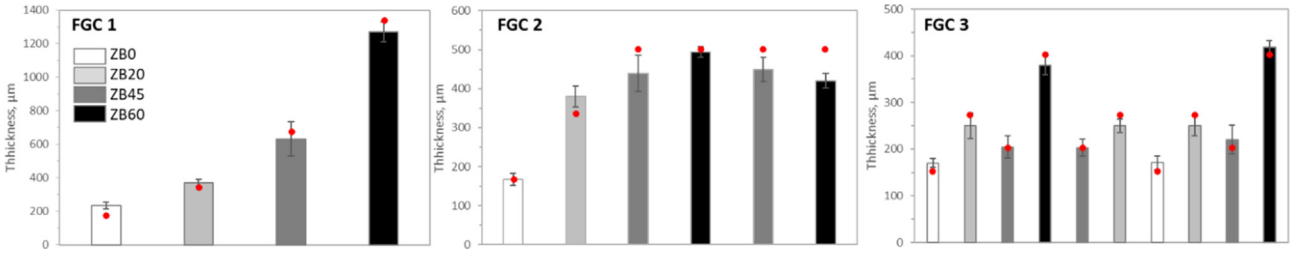

Fig. 8. Actual layer thickness and standard deviation as measured on SEM images on the FGCs by commercial image analysis software overlapped to the target thickness indicated as red dots. (For interpretation of the references to colour in this figure legend, the reader is referred to the web version of this article.)

Table 1
Experimental thermo-mechanical properties of fiber free matrix [29], ZB0, and mono-reinforced standalone materials, ZBX, with X = 20, 45 and 60 vol% short carbon fiber. σ: 4-pt flexural strength, K_{Ic}: CNB fracture toughness, E: Young's modulus, ν: Poisson's coefficient, λ: coefficient of thermal expansion. λ was measured parallel (//) and perpendicular (†) to the direction of the applied pressure.

Property	ZB0	ZB20	ZB45	ZB60
E, GPa	419	335	129	99
ν	0.25	0.10	0.07	0.07
$\lambda_{(25\text{-}1300)}$, $10^{-6}°C^{-1}$	7.430	8.04 (//) 10.58 (†)	6.35 (//) 10.76 (†)	4.57 (//) 13.73 (†)
σ, MPa	600 ± 90	276 ± 13	129 ± 3	154 ± 4
σ1500,MPa	<240 ± 30	–	219 ± 23	241 ± 45
K_{Ic}, MPa·√m	3.93 ± 0.43	4.25 ± 0.07	4.32 ± 0.27	4.68 ± 0.11
K_{Ic} 1500, MPa·√m	–	–	6.09 ± 0.17	6.62 ± 0.75

Table 2
Indentation modulus obtained upon nanoindentation with 500 mN load on each layer of the various FGCs. (FGC 2 not measured).

Modulus [GPa]	ZB0	ZB20	ZB45	ZB60
ZB60/ZB0	192 ± 27	–	–	51 ± 19
ZB60/ZB20	–	439 ± 67	–	101 ± 23
ZB60/ZB45	–	–	169 ± 59	95 ± 25
FGC 1	255 ± 17	346 ± 42	135 ± 42	83 ± 27
FGC 3	302 ± 27	337 ± 82	127 ± 55	90 ± 23

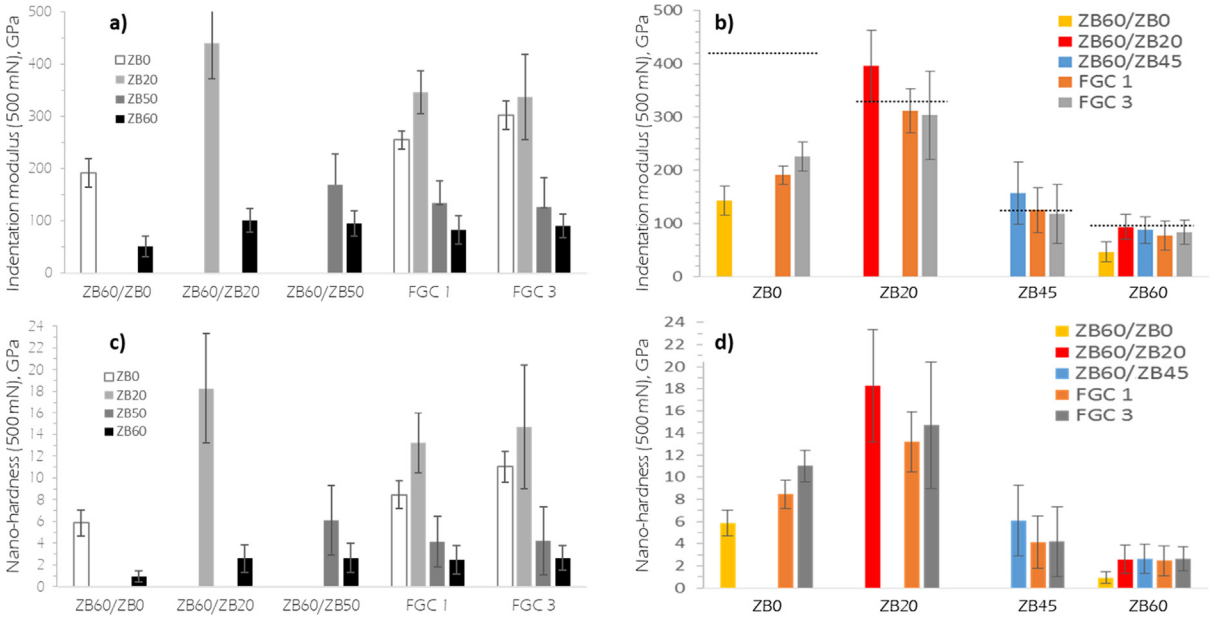

Fig. 9. Plot of the Indentation modulus measured on the different layers of the various FGCs using 500 mN load grouped by a) composite, or by b) layer composition in the various composites. The dotted horizontal lines in b) mark the Young's modulus as measured on the mono-reinforced materials, Table 1. c) and d) are the plots of the measured nano-hardness grouped by material or layer composition, respectively.

was reduced, varying from 395 GPa in the ZB60/ZB20 composite and converging to 303 GPa in FGC 3. For compositions with higher fiber volume fraction, ZB45 and ZB60, the differences between the stiffness values of mono-reinforced materials and those locally measured on the composites notably decreased and were within the standard deviation.

What emerges from this double measure of the stiffness on mono-reinforced standalone composites and local modulus within a complex layered architecture, is that a discrete correspondence can be assessed already for composites containing 20 vol% fiber on, whereas for the bulk fiber-free composition local data are more representative of the final situation.

On the other hand, large variations of the nano-hardness measured in the same nominal composition were instead observed, since hardness is a short-range property and is strongly impacted by the local microstructural features, Fig. 9c,d.

To evaluate the effect of multi-layering, the fracture toughness of the $(AB)_nA$ and complex FGCs was experimentally measured, like summarized in Table 3, and compared to mono-reinforced ZrB_2 composites and to a previously published FGC* [20] as plotted in Fig. 10a as a function of the experimental density.

For the present composites, no delamination or marked step-like fracture was observed, therefore the interfaces between the various layers can be considered strong. Fracture departing from a layer under compression will be hindered as compared to a zone under tension, where the crack will easily propagate.

It can be noticed in Fig. 10a that, in all cases, a toughness increment was recorded as compared to the mono-reinforced materials, [9,10] marked by black indicators. In addition, for FGC 1&2, a further increase as compared to the old generation FGC* [20] was achieved. On the other hand, FGC 3, featured by micro-cracked inner zones, Fig. 7, had the lowest fracture toughness comparable to the $(AB)_nA$ composites, for which only negligible increments were measured.

Another feature worthy of mention was the graceful behavior of all composites, as indicated by the load–displacement curves in Fig. 10c and confirmed by the united bars after both room and high temperature tests, Fig. 10d. The newly developed FGCs simultaneously achieved a higher load before rupture and a more tolerant failure profile, i.e., after the first crack formed, a small drop in load followed and the curve assumed a tail shape typical of stable crack propagation, Fig. 10c. Optical photos of the split bars upon fracture toughness tests at room temperature are shown in Fig. 10f, where increased jagged and irregular fracture profile can be appreciated with increasing differences between adjacent layers.

An estimation of the work of fracture is reported in Table 3 and it ranged from around 210 to 360 J/m^2, thus overpassing by far that of ZrB_2 composites reinforced with 20 vol% SiC chopped fiber, which ranged around 75–114 J/m^2 [32], that of composites reinforced with 20 vol% short carbon fibers of the same nature as those used in this study, around 90 J/m^2 [33], and even the WoF of ZrB_2 containing BN-coated continuous SiC fibers, around 140 J/m^2 [32]. The inelastic WoF, i.e., the area under the curve tail beyond the highest load in Fig. 10c, is a measure of the amount of energy required to propagate a crack after it has been initiated. Thus, while not a measure of K_{Ic}, higher inelastic WoF suggests that

Table 3
Theoretical (ρ_{th}), experimental and relative density (ρ), fracture toughness (K_{Ic}) at room and high temperature measured by CNB and work of fracture (WoF) of the FGCs.

Composite	ρ_{th}, g/cm^3	ρ, g/cm^3	ρ, %	K_{Ic}(RT), MPa·m$^{0.5}$	WoF(RT), J/m^2	K_{Ic}(1500°C), MPa·m$^{0.5}$
ZB60/ZB0	4.63	3.72	80.4	–	–	–
ZB60/ZB20	4.25	4.18	98.4	4.65 ± 0.39	–	–
ZB60/ZB45	3.78	3.61	95.5	4.71 ± 0.17	360 ± 52	5.28 ± 1.28
FGC 1	4.07	3.84	94.4	6.74 ± 0.62	275 ± 41	6.44 ± 1.22
FGC 2	4.12	3.95	95.8	6.90 ± 0.10	294 ± 37	7.72 ± 0.60
FGC 3	4.45	4.28	96.2	4.78 ± 0.33	210 ± 35	8.34 ± 1.54

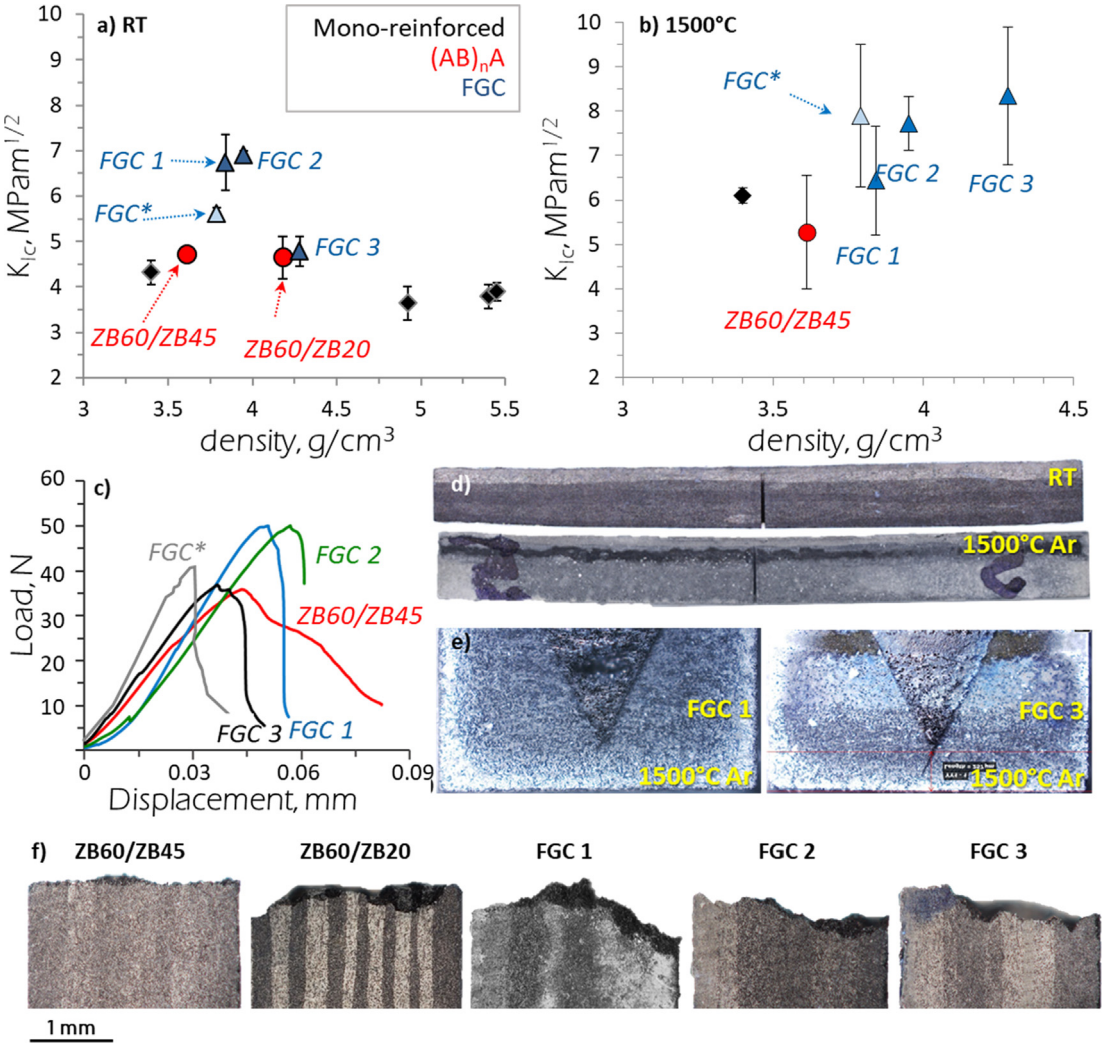

Fig. 10. Experimental fracture toughness of mono-reinforced ZrB_2 composites [9,10], old generation composite *FGC** [20], and present $(AB)_nA$ and *FGCs* as a function of the density tested at a) room temperature and b) at 1500 °C. c) Examples of load–displacement curves upon CNB toughness tests measured at room temperature. d) Photos of unsplit bars upon CNB test at room and high temperature (case of FGC 1). e) Optical images of FGC 1 and FGC 3 upon CNB test at 1500 °C in Ar showing different oxidation damage levels in correspondence of the notch justifying highest values for the FGC 3, owing to a UHTC-richer zone. f) Optical images of the profile of the split CNB bars tested at room temperature showing increased tortuosity for increased difference between adjacent layers.

the biphasic ZB60/ZB45 and the complex FGC 3 are more resistant to catastrophic failure than the other FGCs 1&2.

Fracture toughness tests at 1500 °C in partially protective argon environment generally led to a toughness increase, Fig. 10b, in analogy with similar UHTC-based composites [20,31] and the mono-reinforced materials, Table 1. Moreover, at 1500 °C, all curves and V-cuts were valid, and the specimens remained united after the test, like the example shown in Fig. 10d. For the complex architectures, the toughness trend resulted reversed as compared to the values measured at room temperature, with FGC 3 resulting the toughest composite achieving even 10 $MPa{\cdot}m^{0.5}$. Since the tests were done at sufficiently high temperature where the stresses from multi-layering are supposed to be released, it is proposed that the toughening here observed is attributed to the formation of a thin oxide layer, as ascertained by optical inspection in Fig. 10e. Little oxygen impurities within the testing furnace chamber led to partial oxidation of the composite and the notch was a region susceptible of oxidation. Beside the effect of the newly formed dense oxide scale, with its different thermo-elastic properties [34] as compared to the fiber-reinforced ZrB_2, that induced a compressive state inhibiting crack propagation, likewise in established literature [35], in the zones rich of fiber, carbon fiber were partially consumed leaving voids, whereas in UHTC-rich zones, a ZrO_2-SiO_2 compact zone formed. This hypothesis would justify the highest toughness obtained for the micro-cracked FGC 3 composite.

3.3. Thermo-elastic analysis

The stress fields computed along bars with theoretical size and architecture described in paragraph 2.2 are depicted in Figs. 11–14, where a cooling from the processing temperature of 1900 °C is simulated: negative values indicate compression and positive ones' tension. Although the values might not exactly correspond to the actual stress states, owing to the approximations made, they provide an order of magnitude and give an idea of the stress/tension distribution within the composites. FEM simulations were run using either the elastic modulus measured on the mono-reinforced standalone materials by resonance frequency, or those measured by nanoindentation on each layer of the various composites. As verified in Fig. 9b, remarkable variations of the elastic properties regarded mostly the ZB0 layers. The computation of the stress field along the multi-layered bars have highlighted that the use of input values from nanoindentation resulted in the same trend of stress distribution found using input values from mono-

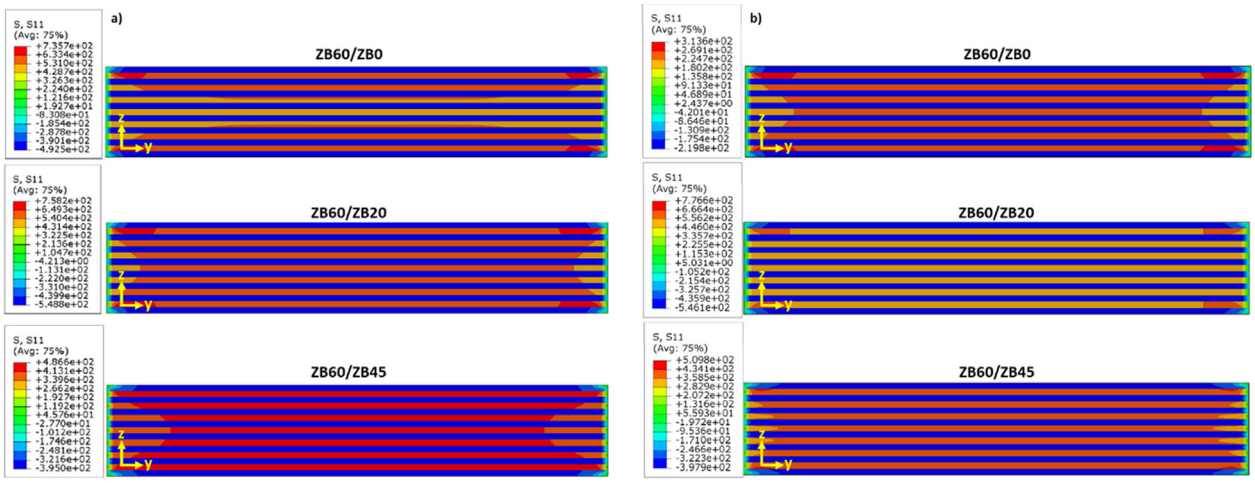

Fig. 11. Simulated thermo-elastic stress fields along a test bar upon cooling the $(AB)_nA$ FGCs. Elastic modulus inputs consider a) those measured on mono-reinforced standalone ceramics, or b) those directly measured by nanoindentation on the FGCs. Negative values, in blue, indicate compression, whereas positive values, in red, represent tension.

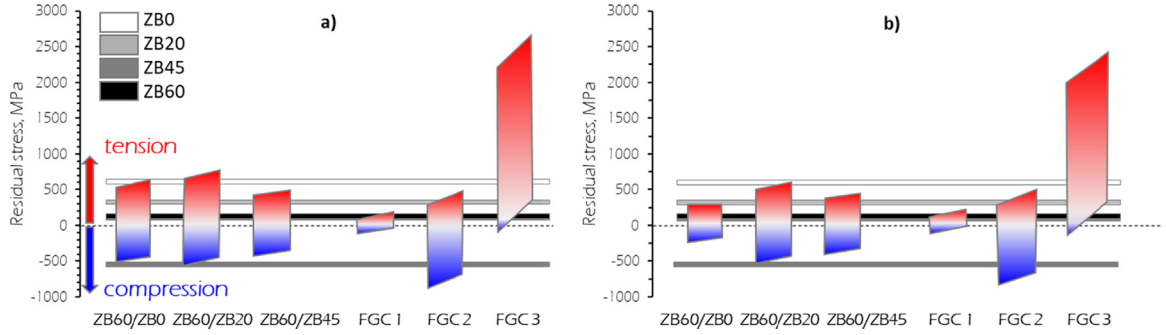

Fig. 12. Plot of residual stresses within the various FGCs in correspondence of the V-notch (see Figs. 11 and 14) overlapped to the measured bending strength of the single ZBX ceramics, or compression strength on ZB45. Simulations are calculated using elastic modulus deriving from a) mono-reinforced standalone ceramics, or b) the various layers within the FGCs by nanoindentation.

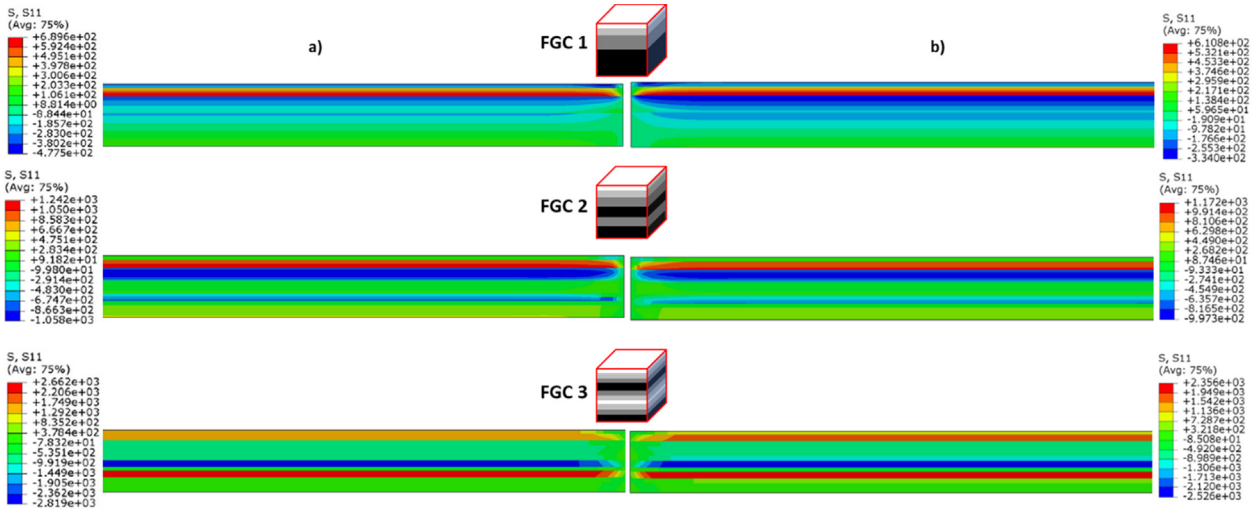

Fig. 13. Simulated thermo-elastic stress fields along the FGCs test bar upon cooling obtained using input values for elastic modulus as measured a) on mono-reinforced standalone ceramics, or b) on each single layer of the FGCs by nanoindentation.

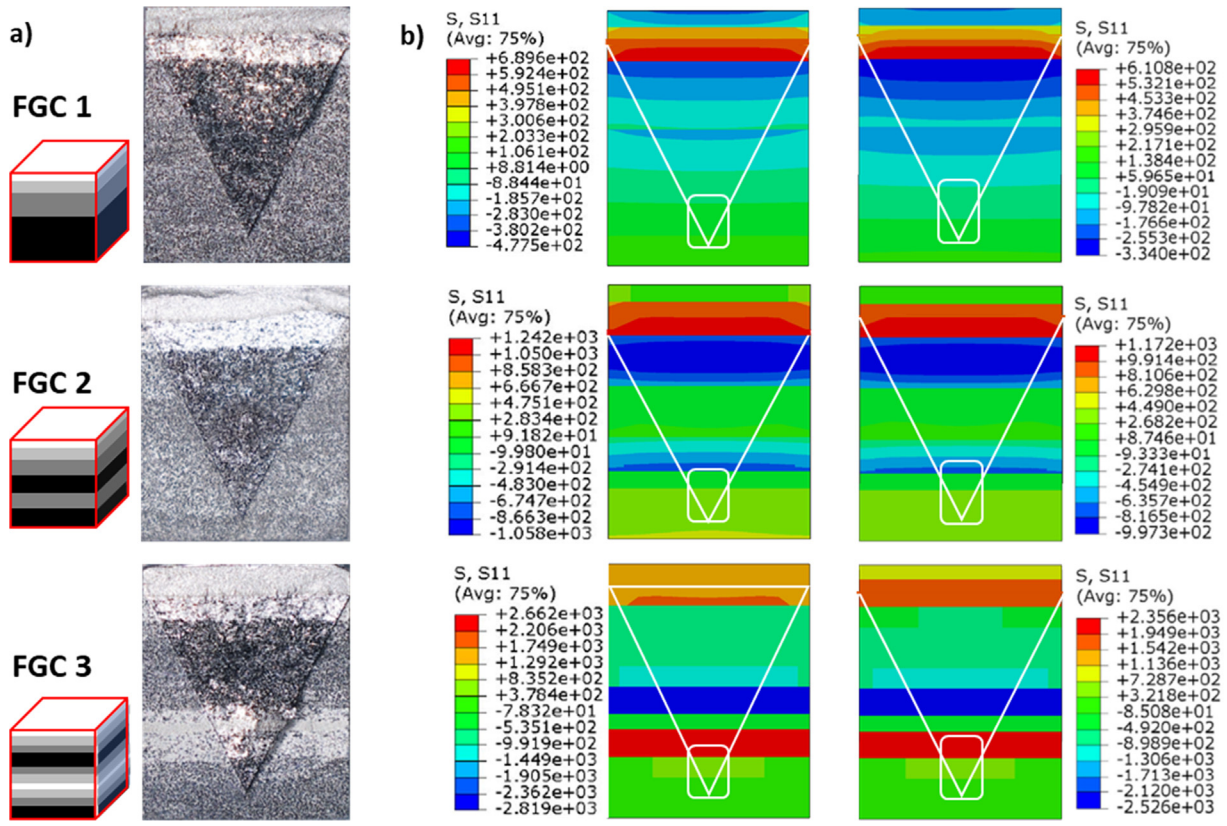

Fig. 14. a) Optical images of the complex V-notch plane section in FGCs fractured bars with b) simulated thermo-elastic stress fields across the test bar where input values for elastic modulus are measured on either mono-reinforced standalone ceramics (left), or by nanoindentation (right) in the various FGCs. The residual stress range in correspondence of the V-tip is highlighted and plotted in Fig. 12.

reinforced standalone ceramics, just the stress intensity jump changed, Fig. 11.

For the $(AB)_nA$ composites, the simulation that used the values of the single ceramics had large differences in both tensional and compressive stresses, Fig. 11a. The thermo-elastic analysis reveals that for the ZB60/ZB0 composite, in the ZB0 layer a traction stress state is present, up to + 633 MPa, whereas in ZB60 an almost constant compression stress state, down to −490 MPa is found. To note that, currently, no compression strength data are available for the mono-reinforced ceramics, unless for ZB45, which was measured to vary from 534 ± 41 to 550 ± 11 MPa, depending on the test orientation, as measured on blocks with size of 4x4x8 mm^3, according to the ISO 17162:2014 standard [36]. The composites with highest fiber fraction, ZB45 and ZB60, were those with the lowest bending strength, 130–150 MPa, therefore, since the compression strength is much higher than the tensile strength for ceramics, we can assume that the compression strength for ZB20 and ZB0 will be at least as high as −550 MPa.

For the ZB60/ZB20 composite, the tensional stress estimates are above the fracture bending strength measured on the bulk single ZB0 ceramic, whereas the compressive stresses are below the compression strength measured on ZB45, and hence also presumably on ZB60. To better visualize if the strength requirement was overpassed or not, Fig. 12 collects the various stress field distributions in correspondence of the V-notch for the various FGCs which are overlapped to the fracture strength of the mono-reinforced composites measured in tension and compression.

Looking at Fig. 12b, where input data from nanoindentation instead considering, the stress field is much reduced and below the fracture strength of both ZB0 and ZB60.

Notably, using the values of the single composites, the threshold strength is often overpassed, Fig. 12a, instead, if we use values from nanoindentation, the stress extension is reduced and below the threshold. We can therefore deduce that the thermo-elastic analysis that used values of the single standalone materials is the theoretical representation of the stress distribution before eventual cracking occurs upon cooling. When the material is cooled to room temperature, diffused cracking has started in the critical layers, Fig. 2, and the corresponding elastic modulus notably reduced, Fig. 9b. Within this picture, data from single ceramics should be used for architecture optimization, since the nanoindentation provides stress fields that are representative of the actual final situation, i.e. upon stress release by cracks creation.

Moving to the ZB60/ZB20 material, the thermo-elastic simulated test in Fig. 11 shows that every ZB20 layer is subjected to a tensional state, as indicated by the orange zones, and ZB60 is subjected to compression. Comparing these fracture threshold range with the experimental values of ZB20 reported in Table 1, the natural development of flaws is plausible also in this composite, whereas ZB60 is only partially touching the compression strength limit, Fig. 12a. In this composite, the differences of stress fields using the two sources of elastic moduli were minimal.

The thermo-elastic analysis for the ZB60/ZB45 composite shows that the stress field goes from tensile zones in ZB45, to compressive zones in ZB60, with only the ZB45 composition exceeding the fracture threshold and so putting forth the natural defect's onset.

From Fig. 12a, the compressive fields developed in the various composites, except for FGC 2, are below the compressive strength threshold (available for ZB45), therefore propagation of cracks in these layers is less likely, but rather naturally occurs in layers under tension.

Moving to the complex architectures, the corresponding computed stress fields are displayed in Fig. 13. To correlate the thermo-elastic stresses computed for each FGC to the actual failure

behavior of the composites, Fig. 14 reports optical pictures of the CNB bars upon test and the stresses distribution in the center of the bar overlapped to the position of the V-notch. The stress range in correspondence of the notch tip is cumulatively visualized in Fig. 12.

In the outmost ZB0 layer of FGC 1, a compression stress state occurs, around −177 MPa, whereas in the ZB20 layer a traction stress state arises. The numerical values estimates are higher than the experimental strengths for ZB20, suggesting presence of defects especially at the interface with the ZB45 layer underneath. On the contrary, between the ZB45/ZB60 layers the stress state computation does not foresee any micro-cracks onset. This architecture was designed to make the notch fall in a slightly compressed zone, green/light blue in Fig. 14b.

In the first two layers of FGC 2, ZB0 and ZB20, a traction stress state arises, suggesting the presence of defects and tensional stresses accumulation at the bottom side of ZB20. Then, starting from the first ZB45 layer and down to the innermost ZB45 one, a compressive state develops instead. In such configuration of stress distribution, the propagation of the defects born in the fiber-poor layers towards the fiber-rich layers might be hindered. The last layer, made of ZB60, is then subjected to a traction stress state and, from a numerical point of view, the strength requirement should be exceeded, Fig. 12. It is worthy to underline that the position of the notch fell in a highly compressed area, like indicated in Fig. 14b.

Lastly, in the outermost ZB0 layer of FGC 3, a traction stress state occurs, exceeding 1 GPa, that justifies the formation of cracks experimentally found, Fig. 7. Then, the five subsequent fiber-rich layers are all subjected to a compressive load suggesting obstruction of crack propagation, especially in the central dark blue zone, reaching compression values close to −2.5 GPa. Afterwards, from the central ZB0 layer to the bottom, all layers are subjected to a load higher than the strength requirement, justifying the observed micro-cracking. In this case, although the notch falls in a favourable zone (green), propagation occurs towards a zone of the composite under too high tensile stresses (red) which weakens the composite, Fig. 14b.

The combination of the measured fracture toughness and of the tensional/compressive states computed is key for optimization of the composite's performances.

The fracture toughness measurements yielded quite a broad range of values at room temperature, from 4.7 $MPa{\cdot}m^{0.5}$ for ZB60/ZB20 to 6.9 $MPa{\cdot}m^{0.5}$ for FGC 2, i.e., lowest when the notch fell in the zero-fiber region and highest when it fell close to fiber-rich regions. What is more, the highest values were obtained when the crack propagated towards a zone under compression, light green to blue.

In the least favorable case, FGC 3, although the notch fell in a zone of compression (green/light blue), propagation occurred towards a zone of the composite under too high tensile stresses (orange/red) which embrittled the composite, Fig. 14b.

The good combination of these experimental and computational results puts forth the employ of numerical modelling as an advantageous route to decrease the resources, time and cost efforts for the design of functionally graded UHTCs also in view of preparation of more complex shapes.

4. Conclusions

Functionally graded (FG) ultra-high temperature ceramics based on ZrB_2-SiC and with variable contents of short carbon fiber were designed to maximize the failure tolerance and the ablation resistance capability and to minimize the weight.

Simple $(AB)_nA$ and more complex asymmetric architectures were prepared by hot pressing, characterized from the microstructural and mechanical points of view, and the thermo-elastic fields resulting from layering upon cooling from the processing temperature were evaluated by finite element modeling. As elastic modulus inputs, both values obtained on mono-reinforced standalone materials, using the resonance frequency, and directly measured by nanoindentation on the various layers of the FG architectures were considered. The methodology applied in this work highlighted that the former represents the ideal situation with crack-free layers, and it can be used for the FG architecture preliminary design, whereas the latter reproduces the real situation of the sintered ceramics including the actual flaws formed upon exceeding the strength requirement and can be used to estimate the effective toughening due to layering.

Keeping a density below 4 g/cm^3, the highest fracture toughness of 7 $MPa{\cdot}m^{0.5}$ was achieved at room temperature when crack propagated towards a highly compressed zone. The fracture toughness was also evaluated up to 1500 °C in partially protective environment and values up 10 $MPa{\cdot}m^{0.5}$ were reached when the notch fell in a UHTC-rich area, owing to the formation of a dense oxide layer which applied a compressive stress that obstructed the crack advancement.

A clear correspondence between thermo-elastic fields and actual failure behavior was obtained, thus demonstrating the tunable flexibility and cost-effectiveness of the method to explore complex architectures that join dissimilar materials for enhanced properties.

Data availability

The data that has been used is confidential.

Declaration of Competing Interest

The authors declare that they have no known competing financial interests or personal relationships that could have appeared to influence the work reported in this paper.

Acknowledgements

Research was jointly sponsored by the U.S. Army DEVCOM and by the U.S. ONR and was accomplished under the Cooperative Agreement n. W911NF-19-2-0253 with Amanda Napier and Eric Wuchina as contract monitors. The views and conclusions contained in this document are those of the authors and should not be interpreted as representing the official policies, either expressed or implied, of the U.S. Army DEVCOM, U.S. ONR or the U.S Government. The U. S. Government is authorized to reproduce and distribute reprints for Government purposes notwithstanding any copyright notation herein. Part of the activity was financed by the NATO Science for Peace and Security Programme under grant MYP-G5767 (SUSPENCE). Nanoindentation tests were supported by The Spanish Ministry of Science, Innovation and Universities through the grant PGC-2018-096855-B-C41.

Data availability

The raw and processed data required to reproduce these findings cannot be shared at this time due to legal or ethical reasons.

The authors certify that they have NO affiliations with or involvement in any organization or entity with any financial interest or non-financial interest in the subject matter or materials discussed in this manuscript.

References

[1] W.G. Fahrenholtz, E.J. Wuchina, W.E. Lee, Y. Zhou, A.C. Di, Ultra-High Temperature Ceramics: Materials for Extreme Environment Applications, John Wiley & Sons Inc., Hoboken, New Jersey, 2014. doi: 10.1002/9781118700853.

[2] S.R. Levine, E.J. Opila, M.C. Halbig, J.D. Kiser, M. Singh, J.A. Salem, «Evaluation of ultra-high temperature ceramics for aeropropulsion use», J. Eur. Ceram. Soc. 22 (fasc. 14–15) (2002) pp. 2757–2767, doi: 10.1016/S0955-2219(02)00140-1.

[3] E.J. Wuchina, E. Opila, M. Opeka, W.G. Fahrenholtz, I. Talmy, «UHTCs: Ultra-high temperature ceramic materials for extreme environment applications», Electrochem. Soc. Interfaces 16 (2007) pp. 30–36.

[4] J.-L. Shi, «High-Temperature Structural Ceramics: Recent Progress in China», Adv. Mater. 11 (fasc. 13) (1999) pp. 1103–1109.

[5] Y. Zhou, H. Hyuga, D. Kusano, Y.I. Yoshizawa, K. Hirao, «A tough silicon nitride ceramic with high thermal conductivity», Adv. Mater. 23 (fasc. 39) (2011) pp. 4563–4567, doi: 10.1002/ADMA.201102462.

[6] P.A. Williams, R. Sakidja, J.H. Perepezko, P. Ritt, «Oxidation of ZrB_2 –SiC ultra-high temperature composites over a wide range of SiC content», J. Eur. Ceram. Soc. 32 (2012) 3875–3883.

[7] K. Shugart, S. Liu, F. Craven, E. Opila, «Determination of Retained B_2O_3 Content in ZrB_2-30 vol% SiC Oxide Scales», J. Am. Ceram. Soc. 98 (fasc. 1) (2015) pp. 287–295.

[8] M. Estili, A. Kawasaki, Y. Sakka, «Highly concentrated 3D macrostructure of individual carbon nanotubes in a ceramic environment», Adv. Mater. 24 (fasc. 31) (2012) pp. 4322–4326, doi: 10.1002/ADMA.201201134.

[9] L. Silvestroni, E. Landi, K. Bejtka, A. Chiodoni, D. Sciti, «Oxidation behavior and kinetics of ZrB_2 containing SiC chopped fibers», J. Eur. Ceram. Soc. 35 (fasc. 16) (2015), doi: 10.1016/j.jeurceramsoc.2015.07.024.

[10] L. Silvestroni, L. Pienti, S. Guicciardi, D. Sciti, «Strength and toughness: The challenging case of TaC-based composites», Compos. Part B: Eng. 72 (2015), doi: 10.1016/j.compositesb.2014.11.043.

[11] D. Sciti, S. Guicciardi, L. Silvestroni, «Are short Hi-Nicalon SiC fibers a secondary or a toughening phase for ultra-high temperature ceramics?», Mater. Des. 55 (2014), doi: 10.1016/j.matdes.2013.10.019.

[12] S. Mungiguerra, G.D. Di Martino, R. Savino, L. Zoli, L. Silvestroni, D. Sciti, «Characterization of novel ceramic composites for rocket nozzles in high-temperature harsh environments», Int. J. Heat Mass Transfer 163 (2020), doi: 10.1016/j.ijheatmasstransfer.2020.120492.

[13] Y. Zhang, L. Zhang, L. Cheng, Y. Xu, «Tensile behavior and microstructural evolution of a carbon/silicon carbide composite in simulated re-entry environments», Mater. Sci. Eng. A, 473(fasc. 1–2) (2008) pp. 111–118, doi: 10.1016/j.msea.2007.05.015.

[14] D. Zhang, P. Hu, S. Dong, C. Fang, J. Feng, X. Zhang, «Microstructures and mechanical properties of Cf/ZrB_2-SiC composite fabricated by nano slurry brushing combined with low-temperature hot pressing», J. Alloys Compound. (2019), https://doi.org/10.1016/j.jallcom.2019.03.147.

[15] L. Náhlík, L. Šestáková, P. Hutař, R. Bermejo, «Prediction of crack propagation in layered ceramics with strong interfaces», Eng. Fracture Mech. 77(fasc. 11) (2010), pp. 2192–2199.

[16] N.A. Orlovskaya, J. Kuebler, V.I. Subotin, M. Lugovy, «High Toughness Ceramic Laminates by Design of Residual Stresses», MRS Online Proceedings Library, vol. 702, p. 871, 2001.

[17] V.M. Sglavo, M. Bertoldi, «Design and production of ceramic laminates with high mechanical reliability», Compos. Part B: Eng. 37(fasc. 6) (2006) pp. 481–489.

[18] R. Bermejo, Y. Torres, A.J. Sánchez-Herencia, C. Baudín, M. Anglada, L. Llanes, «Residual stresses, strength and toughness of laminates with different layer thickness ratios», Acta Materialia 54(fasc. 18) (2006) pp. 4745–4757.

[19] L. Silvestroni, C. Capiani, D.D. Fabbriche, C. Melandri, «Novel light and tough ZrB_2-based functionally graded ceramics», Compos. Part B: Eng. 99(fasc. Supplement C) (2016) 321–329, https://doi.org/10.1016/j.compositesb.2016.06.001.

[20] L. Silvestroni, C. Melandri, V. Venkatachalam, J. Binner, D. Sciti, «Merging toughness and oxidation resistance in a light ZrB_2 composite», Mater. Des. 183 (fasc. 5) (2019) p. 108078.

[21] D. Kokkinis, F. Bouville, A.R. Studart, «3D Printing of Materials with Tunable Failure via Bioinspired Mechanical Gradients», Adv. Mater. 30(fasc. 19) (mag. 2018), doi: 10.1002/ADMA.201705808.

[22] D.S.J. Al-Saedi, S.H. Masood, M. Faizan-Ur-Rab, A. Alomarah, P. Ponnusamy, «Mechanical properties and energy absorption capability of functionally graded F2BCC lattice fabricated by SLM», Mater. Des. 144 (2018) pp. 32–44, doi: 10.1016/j.matdes.2018.01.059.

[23] K. Li, et al., «A functionally graded material design from stainless steel to Ni-based superalloy by laser metal deposition coupled with thermodynamic prediction», Mater. Des. 217 (2022), p. 110612, doi: 10.1016/j.matdes.2022.110612.

[24] E. Stavroulakis, S. Irukuvarghula, E. Pickering, D. Stewart, M. Preuss, «Fundamental aspects of functional grading via powder hot isostatic pressing – Development of microstructure and diffusional processes», Mater. Des. 215 (2022) p. 110437, doi: 10.1016/j.matdes.2022.110437.

[25] M. Rühle, Microscopy of structural ceramics, Adv. Mater. 9 (fasc. 3) (1997) 195–217, https://doi.org/10.1002/ADMA.19970090304.

[26] F. De Bianchi, S.A. Ponnusami, L. Silvestroni, A.M. Grande, «Thermo-elastic properties in short fiber reinforced ultra-high temperature ceramic matrix composites: characterization and numerical assessment», Mater. Today Commun. 29 (2021) 102754, https://doi.org/10.1016/j.mtcomm.2021.102754.

[27] W.C. Oliver, G.M. Pharr, «An improved technique for determining hardness and elastic modulus using load and displacement sensing indentation experiments», J. Mater. Res. 7 (1992), pp. 1564–1582.

[28] D.G. Munz, J.L. Shannon, R.T. Bubsey, «Fracture toughness calculation from maximum load in four point bend tests of chevron notch specimens», Int. J. Fract. 16 (1980), fasc. 3, 1980, doi: 10.1007/BF00013393.

[29] F. Monteverde, S. Guicciardi, A. Bellosi, «Advances in microstructure and mechanical properties of zirconium diboride based ceramics», Mater. Sci. Eng. A 346 (2003) 310–319, doi: 10.1016/S0921-5093(02)00520-8.

[30] «www.ngfworld.com».

[31] S. Mungiguerra, L. Silvestroni, R. Savino, L. Zoli, B. Esser, M. Lagos, D. Sciti, Qualification and reusability of long and short fibre-reinforced ultra-refractory composites for aerospace thermal protection systems, Corros. Sci. 195 (2022) 109955.

[32] L. Silvestroni, D. Sciti, G.E. Hilmas, W.G. Fahrenholtz, J. Watts, «Effect of a weak fiber interface coating in ZrB_2 reinforced with long SiC fibers», Mater. Des. 88 (2015), https://doi.org/10.1016/j.matdes.2015.08.105.

[33] L. Silvestroni, D. Dalle Fabbriche, C. Melandri, D. Sciti, «Relationships between carbon fiber type and interfacial domain in ZrB_2-based ceramics», J. Eur. Ceram. Soc. 36 (2016) fasc. 1, pp. 17–24, doi: 10.1016/j.jeurceramsoc.2015.09.026.

[34] A.M. Alper, High Temperature Oxides: Oxides of Rare Earths, Titanium, Zirconium, Hafnium, Niobium and Tantalum, Part 2. Elsevier B.V., 2013.

[35] B. Basu, T. Venkateswaran, D.Y. Kim. "Microstructure and Properties of Spark Plasma-Sintered Zr02-ZrB 2 Nanoceramic Composites" in "Progress in Nanotechnology: Processing", pp. 455-462, by The American Ceramic Society (2009) John Wiley Sons, Inc. ISBN: 9780470588246, doi:10.1002/9780470588246.

[36] L. Silvestroni, et al., «C3harme Project, Deliverable 3.1: Thermomechanical properties: Process/microstructure/properties relationship», Faenza, ITALY, 2018.